1 **Metaschoepite dissolution in sediment column systems – implications for uranium**
2 **speciation and transport**
3

4 William R. Bower[1,2,3], Katherine Morris[2], Francis R. Livens[1,2], J. Frederick W. Mosselmans[4], Connaugh M.

5 Fallon[1,2,3], Adam J. Fuller[1], Louise Natrajan[1], Christopher Boothman[2], Jonathan R. Lloyd[2], Satoshi

6 Utsunomiya[5], Daniel Grolimund[6], Dario Ferreira Sanchez[6], Tom Jilbert[7], Julia Parker[4], Thomas S. Neill[2],

7 Gareth T. W. Law[1,3*]

8

9 1. Centre for Radiochemistry Research, School of Chemistry, The University of Manchester, Manchester,

10 UK, M13 9PL.

11 2. Research Centre for Radwaste Disposal and Williamson Research Centre, School of Earth and

12 Environmental Sciences, The University of Manchester, Manchester, UK, M13 9PL.

13 3. Radiochemistry Unit, Department of Chemistry, The University of Helsinki, Helsinki, Finland, 00014.

14 4. Diamond Light Source, Harwell Science and Innovation Campus, Didcot, UK, OX11 0DE.

15 5. Kyushu University, Department of Chemistry, 744 Motooka, Nishi-ku, Fukuoka, Japan, 819-0395.

16 6. Swiss Light Source, Paul Scherrer Institute, Villigen, Switzerland, 5232.

17 7. Ecosystems and Environmental Research Programme, Faculty of Biological and Environmental Sciences,

18 The University of Helsinki, Helsinki, Finland, 00014.

19 *Corresponding author: gareth.law@helsinki.fi

20

ABSTRACT

Metaschoepite is commonly found in U contaminated environments and metaschoepite-bearing wastes may be managed via shallow or deep disposal. Understanding metaschoepite dissolution and tracking the fate of any liberated U is thus important. Here, discrete horizons of metaschoepite ($UO_3 \bullet nH_2O$) particles were emplaced in flowing sediment/groundwater columns representative of the UK Sellafield site. The column systems either remained oxic or became anoxic due to electron donor additions, and the columns were sacrificed after 6- and 12-months for analysis. Solution chemistry, extractions, and bulk and micro-/nano-focus X-ray spectroscopies were used to track changes in U distribution and behavior. In the oxic columns, U migration was extensive, with UO_2^{2+} identified in effluents after 6-months of reaction using fluorescence spectroscopy. Unusually, in the electron-donor amended columns, during microbially-mediated sulfate reduction, significant amounts of UO_2-like colloids (>60% of the added U) were found in the effluents using TEM. XAS analysis of the U remaining associated with the reduced sediments confirmed the presence of trace U(VI), non-crystalline U(IV), and biogenic UO_2, with UO_2 becoming more dominant with time. This study highlights the potential for U(IV) colloid production from U(VI) solids under reducing conditions and the complexity of U biogeochemistry in dynamic systems.

INTRODUCTION

Uranium (U) has been released into the environment through mining activities, weapons use, and *via* authorized discharges and accidents at nuclear sites.[1-5] It is typically the largest radionuclide by mass in many higher activity radioactive wastes that will be managed via geological disposal,[6] where U exists in a range of chemical forms.[7] Uranium is radiotoxic, chemotoxic, long-lived (^{235}U half-life = 703.8 x 10^6 years, ^{238}U 4.468 x 10^9 years), and persists in the subsurface; thus, it poses a significant environmental and human health risk.[8,9] As such, understanding U behavior in the geosphere is essential.

Uranium is redox-active and its speciation typically controls its solubility and hence mobility. In oxic environments, relatively soluble complexes of U(VI) are typically present.[5] Under anoxic conditions, lower solubility U(IV) species tend to dominate, with reaction end-products including UO_2 and poorly-crystalline U(IV).[10-12] U(V) species have also been documented in environmental studies, but it typically disproportionates.[13,14] Uranium also readily sorbs to a range of minerals (e.g. Fe/Mn-oxy(hydr)oxides, -sulfides, or phyllosilicates)[15-21] and cell surfaces,[22,23] or it can become incorporated into the lattices of neo-forming mineral phases.[24,25] Interestingly, incoperation of U(V) into neo-forming Fe oxy(hydr)oxides appears to stabilise its redox state.[24,26]

Overall, U(VI) reduction, sorption, or incorporation reactions in the geosphere can limit U migration in the environment, but to date, U biogeochemistry studies have largely focused on mechanisms controlling U(VI)$_{(aq)}$ removal from solution (for example, see the review of Newsome et al., 2015).[5] However, U(VI) solids have also been released to the environment (often in particulate form), or they can concentrate naturally (e.g. from U ores, placer deposits etc.). Our understanding of how these U solid phases behave in the environment, and how they contribute to U transport is not well defined.

Metaschoepite (a U(VI) oxide) is a primary product of depleted uranium munition corrosion in former war zones (e.g. Gulf and Balkan Wars) and at military test sites.[27-30] It also forms upon oxidation of UO_2 in the environment,[31,32] and UO_2 can be formed at U contaminated sites *during* U(VI)$_{(aq)}$ biostimulation,[5] or be dispersed in the environment during mining activities or through nuclear accidents.[1,18,32,33] Large volumes of

61 uranium wastes, that include significant amounts of metaschoepite, may also be managed by either shallow

62 or deep disposal in the UK.[7,34] Despite this, the environmental behavior of metaschoepite, and its impact on

63 U transport in complex, dynamic environmental systems is poorly constrained.

64 The objective of this study was therefore to track the stability of metaschoepite and the biogeochemistry of

65 any liberated U in complex sediment/groundwater systems, under realistic environmental conditions (i.e.

66 flowing groundwater, variable redox, dynamic sediment microbial communities). To do this, sediment

67 columns representative of the UK Sellafield Ltd. site were doped with discrete horizons of metaschoepite

68 particles. The metaschoepite was then subjected to groundwater flow for periods of up to 12-months; here,

69 the columns either remained oxic, or became progressively reducing due to the addition of electron donors.

70 Column effluent sampling during the experiments showed that metaschoepite was readily dissolved;

71 however, in the electron donor amended system, there was significant production of UO_2-like colloids during

72 microbially-mediated sulfate reduction. Sacrificial sampling of the sediments after 6- and 12-months of

73 reaction and bulk, micro- and nano-focus XAS and XRF analyses was used to track changes in solid U

74 speciation over time. Here, in oxic sediments U(VI) binding to Fe-bearing mineral phases was shown to be

75 important for longer term U(VI) retention. In the reducing sediments, a mix of non-crystalline U(IV) and

76 biogenic UO_2 governed U retention, but UO_2 appeared to be more prevalent over time. Trace U(VI) was also

77 detected in the reducing sediments, despite 10-months of sustained sulfate-reduction. The study highlights

78 the potential for U(IV) colloid production from U(VI) solids under anoxic conditions and the complexity of U

79 speciation in sediment systems.

MATERIALS AND METHODS

Metaschoepite Source

Synthetic metaschoepite powder was used as a metaschoepite source in sediment column studies. Prior to use, the metaschoepite was sieved to 25-50 μm; the "particles" in this size fraction were aggregates of micron-scale platelets that formed electrostatically bound clusters. Uranium comprised 77 wt % of the solid, yielding an average stoichiometry of $UO_3 \bullet 1.3H_2O$. Further detail on the metaschoepite is provided in the SI (Section 1).

Sediment and Synthetic Groundwater

Sediment representative of the UK Sellafield Ltd. site subsurface was collected from a well-characterized field site in Cumbria[35] (SI Section 2). The sediments were sampled from the unsaturated near surface (~5-10 cm depth) and were confirmed to be oxic at the point of collection, and at the start of experiments (>97% of the 0.5 N HCl extractable Fe was present as Fe(III)). Prior to use in experiments, the sediment was sealed and stored at 4°C for <2-months under a normal atmosphere. Autoclaved synthetic groundwater representative of the Sellafield region,[36,37] was used in the experiments (Table S1).

Column Design and Experimental Approach

A sediment / flowing groundwater column system was used so that the metaschoepite would be reacted under conditions that are representative of those found in the environment, for example, where solid contaminants would likely undergo gradual burial in soils / sediments, and experience water flow, ephemeral redox conditions, and the influence of dynamic microbial communities. A schematic of the column set-up is provided in the SI (Figure S4). The columns were made from acrylic tubing (18 x 4 cm; total volume ~214 cm^3) and were packed with 240 g (12 cm vertical, ~151 cm^3) of sediment. 227 mg of metaschoepite (174 mg U) was added into a 2 cm (vertical) horizon of the sediment (40 g sediment). The columns were terminated at each end with layers of quartz sand (1 cm vertical) and glass wool (2 cm vertical), and then sealed with Duran^{TM} GL45 screwcaps with GL14 connectors. This set-up meant that the metaschoepite horizon was

104 placed 5 cm above the groundwater inlet, and 2 cm from the sediment base (see Figure S4). A peristaltic

105 pump (Watson-Marlow 205-U) was used to pump synthetic groundwater into the base of the columns, with

106 effluents then collected from the top of the columns. The groundwater pumping rate was 1.8 ± 0.2 mL hr^{-1}

107 (1.14 x 10^{-6} m s^{-1}).[37]

108 Two groundwater treatments were used: (i) oxic, and (ii) electron-donor amended. For the oxic treatment,

109 an air bubbler was used to maintain O_2 in the groundwater; for the electron-donor amended treatment, 1

110 mM (total) of acetate and lactate (50:50) was added and the groundwater was sparged with N_2 (30 min L^{-1}).

111 Prior work with these sediments has shown that similar electron-donor addition readily promotes

112 microbially-mediated bioreduction.[35,37,38] Throughout the experiment, the pH of the influent groundwaters

113 was held between 7.2 and 7.4 via HCl addition. In the groundwater reservoirs, the concentrations of NO_3^-,

114 SO_4^{2-}, and electron-donors (when present) remained within 5% of the starting concentrations between

115 weekly groundwater reservoir exchanges. Controls (systems with identical sediment/groundwater but

116 without any added metaschoepite) were also run.

117 **Sampling, Column Sacrifice, and Geochemical Characterization**

118 Duplicate sets of columns were reacted for 6- and 12-months. During this period, effluent samples were

119 collected at intervals by inserting a syringe into a port at the top of the column, with samples collected under

120 flowing Ar. The solutions were then centrifuged (5 minutes, 1.44 x 10^4 g) and the resulting supernatant was

121 monitored for changes in pH, as well as the concentrations of NO_3^-, SO_4^{2-}, Fe, Mn, and U to track microbially-

122 mediated terminal electron accepting processes, changes in sediment geochemistry, and U dissolution/

123 migration from the metaschoepite source. Effluent pH was measured using calibrated electrodes (Mettler-

124 Toledo). Solution concentrations of NO_3^-, SO_4^{2-}, and Br$^-$ (inert tracer) were measured by ion chromatography

125 (Dionex DX120) on filtered (< 0.2 μm PES) samples. Iron, Mn, and U concentrations were measured by ICP-

126 MS (Agilent 7700x) from acidified (2% HNO_3) samples.

127 At experimental end-points (182- and 364-days), columns were uncapped under an Ar atmosphere and sub-

128 cores (18 x 1.5 cm) were taken along the length of each column using thin-walled Al tubes. The sub-cores

129   were immediately flash-frozen in liquid N_2 to preserve the sediment matrix, and then stored under Ar at -80°C

130   before further work. One sub-core was extruded and sectioned at 0.5 cm intervals; the resulting sections

131   were then digested in boiling *aqua regia* for elemental analysis by ICP-AES (Perkin-Elmer Optima 5300), or

132   leached in 0.5 N HCl for 60 minutes to estimate the proportion of bioavailable Fe(II) in the sediments.[39]

133   Sections were also taken and kept frozen (-80°C) for bulk U L_{III}-edge XAS measurements. The other sub-core,

134   which had small perforations in the Al tubing to allow fluid exchange, was resin embedded with Spurr[TM] resin

135   under Ar, using a method designed to maintain the redox chemistry of the sediment and permit synchrotron

136   X-ray based μ-analysis.[40] The resulting resin-embedded core was then cross-sectioned, and 100 μm thick

137   polished sections were prepared and mounted on quartz wafers for subsequent autoradiography and

138   synchrotron μ-focus analysis.

139   **Bulk and Spatially Resolved XAS/XRF Mapping**

140   Bulk U L_{III}-edge fluorescence XAS data were collected on select samples at 77 K on beamline B18 at Diamond

141   Light Source, UK (Si 111 double-crystal monochromator). Spectra were collected using either a 9 or 36

142   element Ge detector and calibrated using a Y-foil standard.

143   μXRF maps and discrete-area XAS data were collected from resin embedded sediment thin-sections on

144   beamlines I18 at Diamond Light Source and X05-LA at the Swiss Light Source (see SI section 4 for further

145   details). μXRF and XANES maps were collected from wafers (extracted perpendicular from the thin-sections

146   using a focused ion beam) on beamline I14 at Diamond Light Source (SI section 4).

147   **Autoradiography**

148   Autoradiographs, showing the distribution of radioactivity across the polished sections, were collected using

149   a Typhoon[TM] 9410 variable mode imager. Samples were exposed for 24-72 hours to a BAS-IP MS storage

150   phosphor screen (Amersham Biosciences) and scanned at 50 μm resolution.

151   **Fluorescence Spectroscopy**

152 Uranyl emission spectra from selected aqueous samples were collected at 77 K following excitation at 420 nm

153 using a FP920 Phosphorescence Lifetime Spectrometer (Edinburgh Instruments) with a 450 W steady state

154 Xe lamp and a Hamamatsu R928P red-sensitive photomultiplier in air-cooled housing.[41] All spectra were

155 corrected for the detector response and excitation source using the instrument correction files.

Transmission Electron Microscopy

157 TEM imaging with Selected Area Electron Diffraction (SAED) of nano-particulate phases present in effluent

158 samples were performed using a FEI Tecnai TF30 FEG analytical electron microscope with EDX spectrometer.

159 Effluent solutions from the columns were prepared for analysis on holey-carbon TEM grids (Agar Scientific)

160 using the method of Neill et al., (2018).[42] Briefly, 2-3 drops (5 µl) of centrifuged (5 minutes, 1.44×10^4 g)

161 effluent solution were pipetted onto the TEM grid and left to dry under an Ar atmosphere. This process was

162 repeated 2-3 times to accumulate sufficient colloids on the grid to permit analysis. The grid was then gently

163 rinsed with a few drops of isopropyl alcohol and finally fully dried (again under Ar) prior to TEM analysis. TEM

164 images/SAED patterns were processed and indexed using Fiji.[43]

DNA Extraction and Microbial Community Characterization

166 DNA was extracted from select sediment samples from each column system to examine changes in the

167 microbial community structure during experimentation. Further details for microbial community analysis are

168 provided in SI section 5.

169   **RESULTS AND DISCUSSION**

170   **Column Effluent Geochemistry and Microbial Ecology**

171   A pore volume of ~62 mL for the column sediment was calculated from the Br^- tracer analysis (SI section 3).

172   This represented ~35% of the column's volume, giving a flow rate of ~0.7 pore volumes/day. Breakthrough

173   occurred after 112 hours (Figure S5). In all experiments, the effluent pH dropped marginally (lowest ~6.5 in

174   the oxic system) during the first month of reaction, presumably due to sediment buffering (SI Section 6). After

175   1-month, all of the effluents buffered to a pH between 7.5 and 7.9 for the remainder of the experiment, likely

176   due to bicarbonate alkalinity in the influent groundwaters (Table S1) and/or alkalinity generation in the

177   microbially-active sediment. It is unlikely that this small change in pH during the first month of groundwater

178   flow would have had a significant impact upon carbonate complexation of U, metaschoepite dissolution, or

179   mineral surface chemistry in this experiment. Stanley and Wilkin (2019) [44] have demonstrated comparable

180   metaschoepite solubility between pH 6-8.5 in the presence of 1mM sodium bicarbonate.

181   In the columns exposed to oxic groundwater with no added electron-donor (both control and U-containing

182   column systems), negligible changes in groundwater NO_3^-, Mn, Fe, and SO_4^{2-} concentrations occurred (Figure

183   1). This suggests that these systems remained predominantly aerobic during the entire reaction period.

184   Uranium breakthrough from the oxic, metaschoepite amended columns was observed between

185   approximately 136-157-days (90-110 pore volumes; Figure 1D). In comparison, breakthrough of the

186   conservative Br^- tracer occurred after 112 hours (Figure S5), indicating that whilst the metaschoepite was

187   undergoing dissolution, U(VI) transport through the sediment was retarded. The first of two columns for this

188   system was sacrificed for solid phase analysis after 182-days, shortly after the initial U breakthrough (open

189   circles - Figure 1D). Effluent data indicated that after 182-days, ~3% of the initial metaschoepite source U

190   (~5.5 mg) had been eluted from the column via dissolution and groundwater transport (Figure 1). By the

191   experiment end-point (364-days), ~85% of the initial U (~148 mg) had been transported out of the column.

192   The microbial community in this U-doped column system, after 6- and 12-months of oxic groundwater flow,

remained remarkably similar to the microbial community of the fresh sediment, but a slight decrease in the

proportion and diversity of Fe(III)- and sulfate-reducing bacteria was apparent (SI section 5.2).
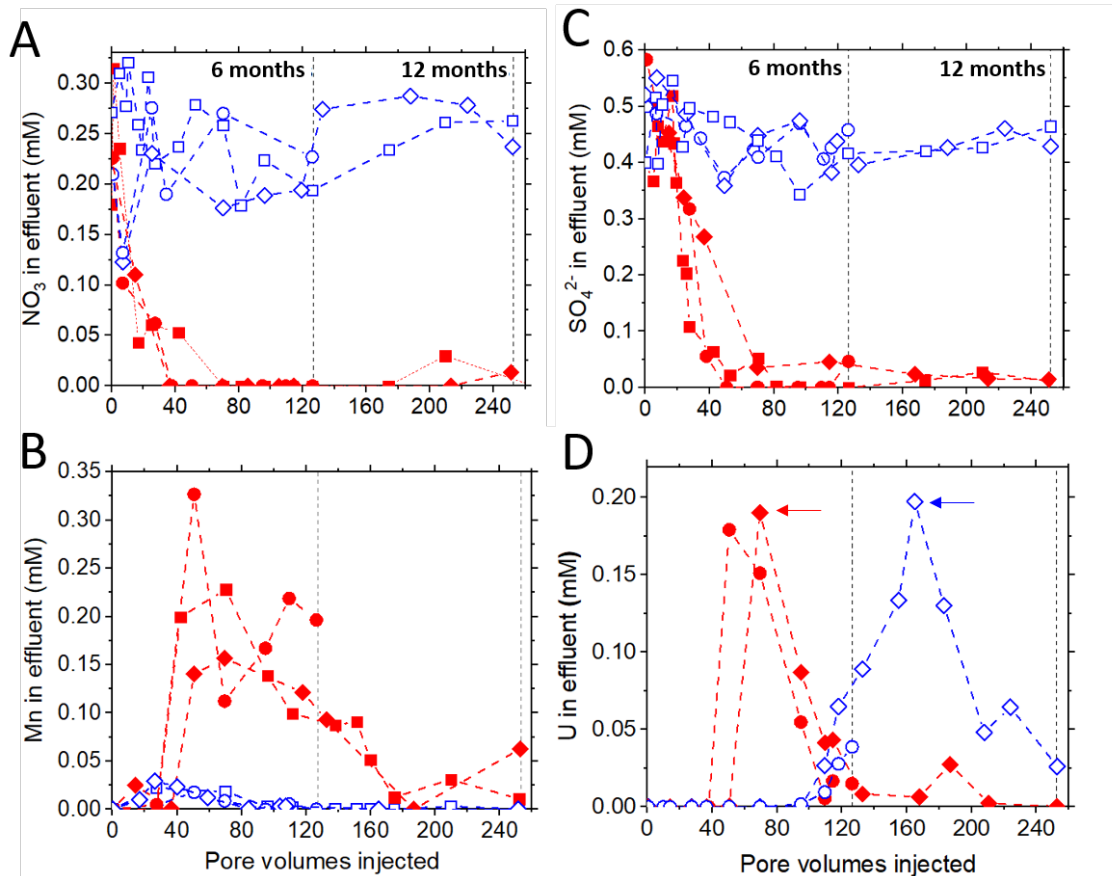
Figure 1. Effluent porewater **(A)** NO_3^-, **(B)** Mn, **(C)** SO_4^{2-}, and **(D)** U for the oxic (no added electron-donor) groundwater system (blue, open symbols), and electron-donor amended groundwater system (red, closed symbols). Squares (open and closed) denote 'control' systems that did not contain any added U, diamonds and circles (open and closed) denote duplicate metaschoepite-doped column systems, where one of each of the duplicate columns was sacrificially sampled after 6-, and then 12-months. No effluent U was detected in the 'control' systems. Vertical dashed lines show timepoints at 6- and 12-months where columns were sacrificed, and solid phase geochemistry and micro-focus analysis was then completed. Arrows indicate the timepoint of effluent sampling for investigations of solution U speciation using TEM and luminescence spectroscopy. Iron was measured in the effluents and was at or close to the method detection limit without a discernible trend, so these data are not presented.

Continuous addition of 0.5 mM acetate and 0.5 mM lactate to the electron-donor amended column system

resulted in a cascade of microbially-mediated terminal electron accepting processes. This was evidenced by

clear trends in the effluent groundwater chemistry (Figure 1) and changes in the microbial community (SI

section 5.2). Dissimilatory NO_3^- reduction was apparent after 14-28-days (~10-20 pore volumes), with NO_3^-,

which was continuously added at 0.3 mM, largely absent in the effluent groundwater after 58-100-days until

the end of the experiment (Figure 1A). Here, it is likely that a stable denitrifying community had developed

within the column, although given the sample resolution for microbial community analysis (SI section 5), it

was not possible to quantify this. As well as denitrification, evidence for metal-reducing conditions was also

observed, with soluble Mn appearing in the effluent after 36-58-days (~20-40 pore volumes) (Figure 1B).

Metal-reducing conditions were also reflected in an increased contribution from dissimilatory metal-reducing

bacteria in the microbial community at 182-days compared to the oxic control and starting material (SI

section 5.2). This was also accompanied by signs of microbially-mediated sulfate reduction, evidenced by a

reduction in the effluent sulfate concentration (continuously added at 0.5 mM) after 35-100-days (~40-70

pore volumes) (Figure 1C) and concurrent blackening of the sediment reflecting Fe-sulfide precipitation

(Figure 4). Indeed, near-total removal of sulfate was maintained from ~3-months until the end of the

experiment (Figure 1). Additionally, after 58-days, the sediment clearly blackened from the base of the

column upwards (Figure 4), indicating that a dynamic and robust sulfate-reducing zone had developed after

the exhaustion of bioavailable NO_3^-, Mn(III/IV), and Fe(III) in parts of the column. The microbial community

analysis data mirrored the column geochemistry, with a marked increase in deltaproteobacteria apparent in

the electron-donor amended columns after 182- and 364-days compared to microbial communities in the

fresh sediment and oxic column system (SI section 5.2; Figure S7). Data showed a relative increase in the

diversity and abundance of sulfate-reducing bacteria and methanogens in the electron-donor amended

columns, alongside a concurrent reduction in certain α-proteobacteria when compared to the fresh sediment

and the oxic column system (Figure S7).

Uranium was also present in the effluent from the electron-donor amended columns between 71-171-days

(~50-120 pore volumes) when clear evidence for strongly reducing, sulfidic conditions was apparent (Figure

1D). Surprisingly, U was eluted earlier than in the oxic column system. Indeed, the amount of U in the

electron-donor amended column effluent was significant, with ~60% (~106 mg) of the added U eluted by

182-days and ~70% (~124 mg) eluted by 364-days.

Uranium Solution Chemistry/ Colloid Analysis

The speciation of U in a sample of the groundwater from the oxic columns (taken after 234-days, U concentration = 0.20 mM) was analyzed using luminescence spectroscopy (Figure 1D and S9). Here, the spectrum was dominated by the characteristic vibrationally resolved emission profile of UO_2^{2+} between 450-600 nm, confirming the solution speciation as dominantly UO_2^{2+}.[41] In contrast, a sample with a similar U concentration (0.19 mM) taken from the electron-donor amended system after 100-days had a 76% reduction in the UO_2^{2+} emission intensity compared to the oxic experiment when the same instrument settings were used (Figure S9). This indicates a reduced $U(VI)_{(aq)}$ contribution to this spectrum compared to the oxic sample.[41] In addition, TEM and SAED analysis of the electron-donor amended effluent after 100-days confirmed the presence of nano-crystalline U-bearing solids (Figure 2), with the SAED data having a structural match to nano-crystalline, biogenic UO_2, as observed by other studies.[10,11,45-50] Taken together, the luminescence and TEM data suggest that the electron-donor amended column effluent contained both aqueous U(VI) and nano-crystalline UO_2-like solids. However, the possible presence of U(VI) in/on the colloids cannot be ruled out, and possible quenching of luminescence from colloid-bound U(VI) may also have contributed to the reduced intensity observed from this sample (Figure S9). The presence of colloids was not tested in the groundwater effluents of the oxic column systems.

The observation of significant UO_2-like colloid production from the metaschoepite source under sulfate reducing conditions is unusual and suggests a significant pathway to U(IV) colloid formation compared to biostimulation studies.[5] Numerous authors have detailed the presence of U(IV)-bearing colloids in laboratory studies.[e.g. 46-52] Suzuki et al., (2002)[46] reported on the formation of biogenic UO_2 colloids from pure-cultures of Desulfosporosinus spp. challenged with $U(VI)_{(aq)}$ and electron donors, and from natural U contaminated sediments. In the pure culture work, the UO_2 colloids (~1-3 nm in diameter) were attached to the bacterial cell walls, indicating that they form at or near to the point of U(VI) bioreduction. Discrete UO_2 colloids and aggregates were also found in this study. Similar work by Lee et al., (2010)[48] documented biogenic UO_2 colloid formation, growth, and aggregation, and TEM analysis demonstrated that biogenic polymers caused the

261   aggregation. UO_2 colloids have also been documented to form on the surface of mackinawite (FeS) in the

262   presence of sulfate-reducing bacteria.[49] In that study,[49] the authors proposed a model where $U(VI)_{(aq)}$ sorbed

263   onto the FeS surface. The U(VI) is reduced to U(IV) via a redox reaction with mineral bound Fe(II); then,

264   microbially-mediated regeneration of the Fe(II) allows for continued U(IV) accumulation on the FeS surface.

265   In turn, thus leads to UO_2 colloid nucleation and growth. Finally, UO_2 colloids have been reported to form

266   from corroding nuclear fuel [e.g. 51] and in experiments where $U(VI)_{(aq)}$ is reacted with highly reactive Fe(II)-

267   bearing minerals.[e.g. 52]

268   In this study, the use of a dynamic column system, combined with the complex biochemistry of the sediments

269   (i.e. competing biotic and abiotic process), means it is not possible to discern how the UO_2-like colloids

270   formed from the metaschoepite in the electron donor amended system. However, the morphology and

271   grainsize of the U(VI)-solid may have played a significant role in forcing colloid formation. For example, rapid

272   metaschoepite dissolution would likely lead to high localised U concentrations for bacteria, or at reactive

273   mineral surfaces, encouraging colloid nucleation and growth.[48-50] In turn, the groundwater flow in the

274   columns could have destabilised colloid growth / aggregation (e.g. concentration or physical effects), and/or

275   the propensity for colloid formation from the metaschoepite source may have outstripped the local supply

276   of aggregating agents, such as biogenic polymers.[48] Recent work in model abiotic systems has also shown

277   that Si can passivate UO_2 colloid surfaces, preventing their aggregation.[42] Si was not added to the synthetic

278   groundwater used in the column experiments (Table S1), but Si would have been present at trace

279   concentrations in the groundwater due to silicate dissolution, and Si was present in the EDX analysis of the

280   UO_2-like colloids (Figure 2). As such, Si may also have also played a role in passivating the surface of the UO_2-

281   like colloids in this study.

282   Irrespective of the mechanisms, extensive UO_2-like colloid formation from metaschoepite under sulfate-

283   reducing conditions is novel and additional work is now required to underpin a mechanistic understanding

284   of their formation and stability. Here, the impact of the U(VI) solid source (e.g. composition, grainsize,

285 morphology), biological interactions with this material, and colloid passivation mechanisms are clear areas

286 for further research.
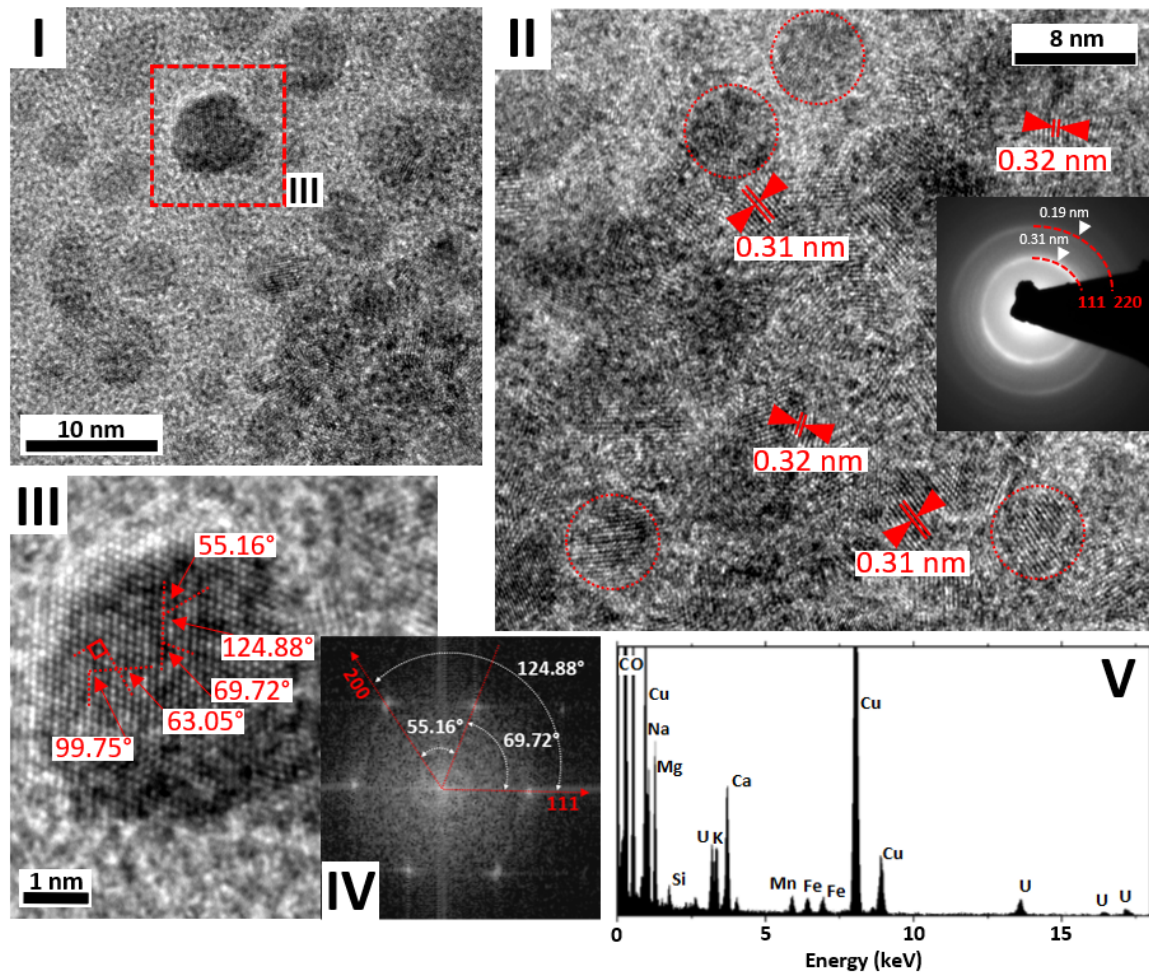
287

288 **Figure 2.** TEM analysis of the nanoparticulate U-bearing phase eluted from the electron-donor amended
289 columns, sampled from effluent groundwater after 70 injected pore volumes (100-days of groundwater
290 flow). **(I-III)** are a series of TEM images at sequentially increasing magnification. Dashed circles in **(II)** denote
291 individual nanoparticles for context. A selected-area electron diffraction (SAED) pattern was collected from
292 **(II)** (see inset) and the two primary reflections have been indexed according to the UO_2 structure. An
293 approximate lattice constant of 0.546 nm was calculated based on SAED analysis, close to that of UO_2 (~0.547
294 nm at ambient temperature).[53] Panel **(III)** shows a high-resolution image of a single colloid, with interplanar
295 angles indicative of the UO_2 structure superimposed. **(IV)** FFT of the area displayed in **(III)**. **(V)** EDX analysis
296 across an aggregation of colloids showed U as one of the most abundant elements, after C and Cu (as inherent
297 components of the TEM grid); further, K, Ca, and Mg were present likely as precipitated salts from the
298 synthetic groundwater. Trace amounts of Mn, Si, and Fe were also measured as expected from complex
299 environmental samples.

300

Acid Extractions and Solid Phase Geochemistry

Sediment samples from two timepoints (182- and 364-days) from each of the oxic and electron-donor amended systems were assessed for bioavailable Fe(II) using 0.5 N HCl extractions (SI Figure S10A).[54] Here both oxic columns showed only trace Fe(II) present in the sediments. This, coupled to the effluent and microbial community data (Figure 1 and SI section 5.2) confirmed that both of the columns remained oxic throughout the experiment. In contrast, after 182-days of electron-donor amendment, this column system showed 75-95% 0.5 N HCl extractable Fe(II) throughout the length of the column (Figure S10A), confirming significant reduction of Fe(III) to Fe(II) and retention of the Fe(II) within the sediments (>90% Fe(II) after 364-days). Additionally, aqua regia extractions confirmed that in both electron-donor amended columns the sediment-associated Mn concentrations were generally lower than comparable oxic columns (Figure S10C), consistent with the observed reductive mobilization of Mn (Figure 1).

Sediment associated U profiles were also measured from a*qua regia* lixiviants and highlighted differences in gross U retention and migration / U loss under the different groundwater treatments. After 182-days flow under oxic conditions, ~70% of the U originally added in the metaschoepite source was recoverable from the column sediments. The U had migrated from the source throughout the entire length of the column (U concentrations varied between 500-1000 mg kg^{-1} up to 6 cm beyond the initial metaschoepite source) (Figure S10D). However, the U mass balance between the sediment extractions and effluents for this system after 182-days was poor (~27% of the added U was unaccounted for). This may reflect heterogeneity in U distribution in the sediments after metaschoepite dissolution (see Figure 3) relative to the coarse-nature of sediment sampling for the aqua-regia extractions. After 364-days under oxic conditions, the solid-phase U concentration had then fallen to between ~150-250 mg kg^{-1} throughout the column (Figure S10D), presumably as a result of the continued dissolution and/or mobilization of particle associated/sediment-bound U(VI). This meant that ~21% of the originally added U remained extractable from the sediment after 1-year of oxic groundwater flow. The U mass balance between the sediment and effluents for this time-point

was better (~106% of the added U accounted for); as such, the majority of the metaschoepite derived U had been transported out of the columns.

In the electron-donor amended columns after 182-days of reaction, the transport of UO_2-like colloids out of the columns (Figure 1D and Figure 2) meant that the total sediment extractable U was significantly lower than its oxic counterpart (only 30% of the U added in the metaschoepite remained in the sediments). This decreased to 21% after 364-days. The U mass balance (sediment extractions and effluents) for the two electron donor amended columns was 90 and 91%, respectively.

Bulk X-ray Absorption Spectroscopy

Select samples were analyzed using bulk U L_{III}-edge XANES and EXAFS. In the oxic systems, at 182-days, the sediments downflow from the initial metaschoepite horizon were sampled. For the bioreduced systems, sediments from both within and downflow of the horizon were sampled at 182- and 364-days (see Figures 3 and 4, SI Figures S11 and S12, Spectra A-E). In order to gain insights into the U oxidation state changes in these complex samples, XANES data were analyzed by Iterative Target Factor Analysis (ITFA) (Figure S11).[55] Sediments from the oxic system showed U(VI) speciation as expected, and sediments from the electron-donor amended systems showed evidence for partial reduction, with ITFA suggesting between 30-80% U(IV) across the samples. Here, the amount of sediment associated U(IV) varied with distance from the metaschoepite source, and the overall proportion of U(IV) increased from 182- to 364-days (Figure S11). For the oxic system, bulk EXAFS fitting parameters and best-fit results confirmed uranyl-like adsorption to the sediment in a sample taken from within the metaschoepite source horizon. Scattering contributions from C and Fe shells indicated uranyl complexation at the surface of Fe-oxy(hydr)oxides in the presence of carbonate. U-C/Fe distances correlate to expected distances for edge sharing carbonato-complexes at the surface of iron oxy(hydr)oxides.[56] Uranyl retention by sediments in this manner is well documented, as U(VI) has been widely shown to sorb (bidentate edge/corner sharing) to a range of Fe/Mn-oxy(hydr)oxides.[21, 56-60] The dominant Fe-oxides in the sediment used in this study are hematite and goethite, which appear to be effective at sorbing U(VI) released from metaschoepite.[56-58]

350   For the electron-donor amended systems, a contribution to the spectra from an axial O shell at ~1.8 Å (uranyl

351   coordination) was varied based on ITFA fitting of the XANES (Table S3) and this approach provided good fits.

352   In the electron-donor amended column system after 182-days of groundwater flow, a uranyl contribution to

353   the bulk EXAFS could still be modelled for samples taken from within the initial metaschoepite source

354   horizon, as well as 3-3.5 cm downflow from the source, but its importance was reduced relative to U(IV)-O

355   coordination (Figure S12, Table S4; spectra B and C). Both spectra could also be modelled with an improved

356   fit that included contributions from Fe and C shells. An oscillation was also visible in the Fourier transform at

357   ~3.8 Å for the 182-day metaschoepite source horizon sample (spectrum B, Figure S12); this may be indicative

358   of a U-U shell from nano-crystalline UO_2,[10,11,46,47] however, the addition of a U-U shell did not yield a significant

359   statistical improvement to the overall model fit for this spectrum.

360   After 364-days of reaction in the electron-donor amended column system (Figure S12, Table S4; spectra D

361   and E), the inclusion of partial uranyl O coordination was still statistically significant, suggesting that even

362   after 10-months under sulfate-reducing conditions, some U(VI) was still present in the sediments. The sample

363   within the original metaschoepite source horizon was modelled with a significant U-U backscatter shell, with

364   3.2 U atoms at 3.84 ± 0.03 Å, suggesting that nano-crystalline UO_2 formation increased with time.[e.g.61]

365   Interestingly, the sample at a greater distance from the original metaschoepite source horizon did not show

366   an improved fit with inclusion of a U-U backscatter shell at ~3.8 Å, suggesting no strong evidence for nano-

367   crystalline UO_2 at distance from the original metaschoepite source horizon.[11,12] The formation of biogenic,

368   non-crystalline U(IV)[10,11] as a U(VI) reductive end-point, separate from that of UO_2 formation, is influenced

369   by the species present in the experiment. The concentration of organic ligands, phosphate and the availability

370   of surfaces of certain Fe(II)-minerals promote formation of non-crystalline U(IV) over UO_2 formation.[10,12,61-64]

371   An Fe backscattering shell could also be modelled for all bulk EXAFS spectra collected from the electron-

372   donor amended columns except for spectrum D (Table S4).

373   Overall, bulk EXAFS fitting for samples from the electron-donor amended column system shows a decrease

374   in U(VI) like coordination with time. After 1-year, at the base of the column where sulfate-reducing conditions

375 have existed for the longest, UO$_2$ ingrowth dominates; with monomeric or non-crystalline U(IV) present

376 further from the initial U and groundwater (and hence sulfate) source.

High Resolution Autoradiography and μ-focus XRF and XAS

378 Data from the oxic column thin-section, sampled after 182-days of groundwater flow, are shown in Figure 3.

379 At the 50 μm pixel resolution provided by the autoradiographs, U migration from the metaschoepite source

380 along the groundwater flow-path is clear. After 182-days in the oxic column, a concentrated zone of

381 radioactivity extends for ~4 cm beyond the metaschoepite source region (Figure 3-II). Beyond this, the activity

382 becomes diffuse. μXRF mapping of selected areas within this zone showed a non-uniform distribution of U

383 throughout the sample. Many areas showed U enrichment in regions also rich in Fe and Mn (e.g. Figure 3;

384 map 1) as well as in the sediment matrix between larger mineral grains (i.e. clay/organic rich areas) (e.g.

385 Figure 3; Panel 4). Clays and organic matter commonly sorb U(VI).[57,65] The area of highest U retention in the

386 thin-section was found along a horizontal, linear feature in the autoradiograph. XRF mapping of this feature

387 (Figure 3; maps 2 and 3) indicates it is a root fragment, due to the presence of life-supporting nutrients such

388 as Cu and Zn[66,67] and consistent with organic material acting as sorption sites for U(VI) in sediments.[68,69]

389 Elemental correlation plots from broad-scale maps (Figure 3-IV) reveal that, of the elements resolvable by

390 μXRF mapping, Fe and Mn show the strongest positive correlations with U in these oxic systems. This is also

391 reflected in bulk EXAFS modelling where fits show Fe backscatters are possible, suggesting sorption to Fe-

392 oxides[59] (Table S4). Zinc and Cu also give an indication of possible U uptake onto organic matter, and a

393 correlation between U and Sr may be indicative of uranyl association with carbonate or clay minerals.[69]

394 μ-focus XANES measurements from the same thin-section (Figure S11, spectra F-I) showed that U(VI) was

395 dominant (>90%) throughout the column. Corresponding μEXAFS measurements could be modelled with

396 uranyl O coordination, similar to that described for the bulk-EXAFS measurement from this column system

397 (see SI section 9 for the full dataset and fitting parameters). Further, μ-focus spectra F-I (Figures 3 and S13;

398 Table S5) could be modelled as uranyl complexes binding to the surfaces of Fe-bearing minerals consistent

399 with U(VI) sorption to Fe-oxides.[55-59] The fit for spectrum I, collected from the root fragment, was significantly

400 improved by the incorporation of a U-C scattering path at 2.91 ±0.02 Å; this may also reflect carbonato-

401 complexed U(VI).[21,56,70] Evidence for a U-C path is also apparent in the Fourier transforms of spectra F and H,

402 but the incorporation of this path was not statistically valid (Table S5).

403 In the electron-donor amended column systems, and consistent with bulk geochemical measurements

404 (Figures 1 and S10), the autoradiographs (Figure 4) displayed a 'patchy' distribution of radioactivity in both

405 the 182- and 364-day columns, highlighting discrete regions of U retention following the onset of sulfate-

406 reducing conditions. XRF maps revealed that after 182-days of groundwater flow, U was found in discrete

407 zones in the sediment matrix (Figure 4, maps 1-4) in a similar manner to that described for the oxic system

408 (U correlated with Fe- and Mn-rich phases, as well as biomarker elements like Zn and Cu). Further, more

409 diffuse areas of U enrichment were found with distance from the metaschoepite source region, as well as

410 additional areas of discrete U enrichment (Figure 4; maps 1-3).
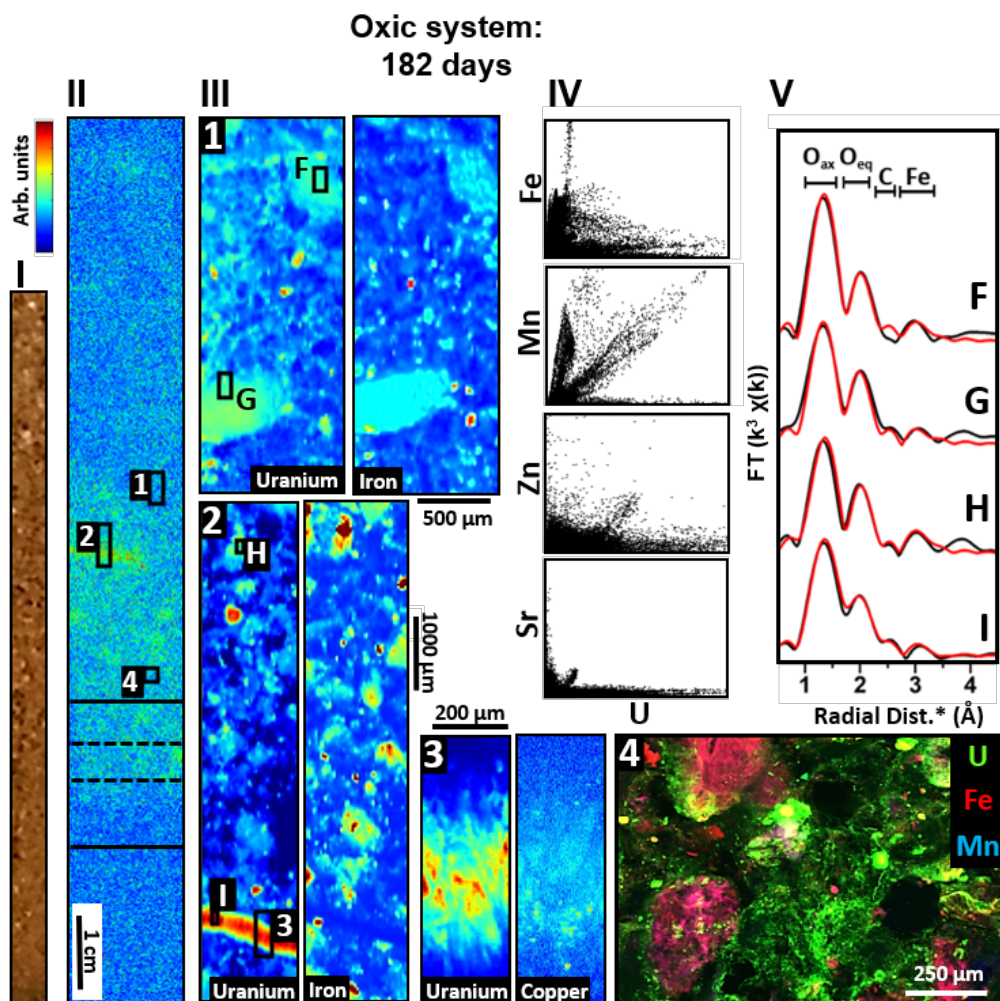
Figure 3. (I) Color photograph (10 cm vertical) of the oxic column after 182-days. Note the uniformity of orange / brown color along the core's length, indicative of Fe(III) dominating throughout. **(II)** Autoradiograph of the resin-embedded, cross sectioned column profile showing radioactivity distribution along the sediment core ('warmer' colors denote higher radioactivity). Solid horizontal lines on the autoradiograph mark the zone of initial metaschoepite particle emplacement. Most of the U had migrated from this zone after 182-days. Dashed horizontal lines denote the horizon sampled for bulk U L_{III}-edge XANES and EXAFS (Spectrum A in relevant Figures and Tables). Numbered boxes within the autoradiographs correspond to μ-focus XRF maps in **(III).** Maps in **(III)** are either displayed as element-specific color panels (where warmer colors denote relative higher concentrations) or as multi-element RGB maps (where green = U, red = Fe, blue = Mn, and color intensity denotes relative proportions of each element). **(IV)** Scatter plots denote correlations between major elements (Fe, Mn, Zn, Sr) and U from broad-scale maps over areas that encompass those shown. Positive correlations denote co-location of the elements at differing concentrations. **(V)** μ-focus (F-I) U L_{III}-edge EXAFS (k^3 weighted Fourier transforms displayed for clarity, full datasets are presented in SI Section 9) from discrete points marked by lettered boxes on the XRF maps. *denotes that the Fourier transform is non-phase corrected. Bracketed regions above the plots show the expected peak positions for O, C and Fe and U scatterers (non-phase corrected).

429
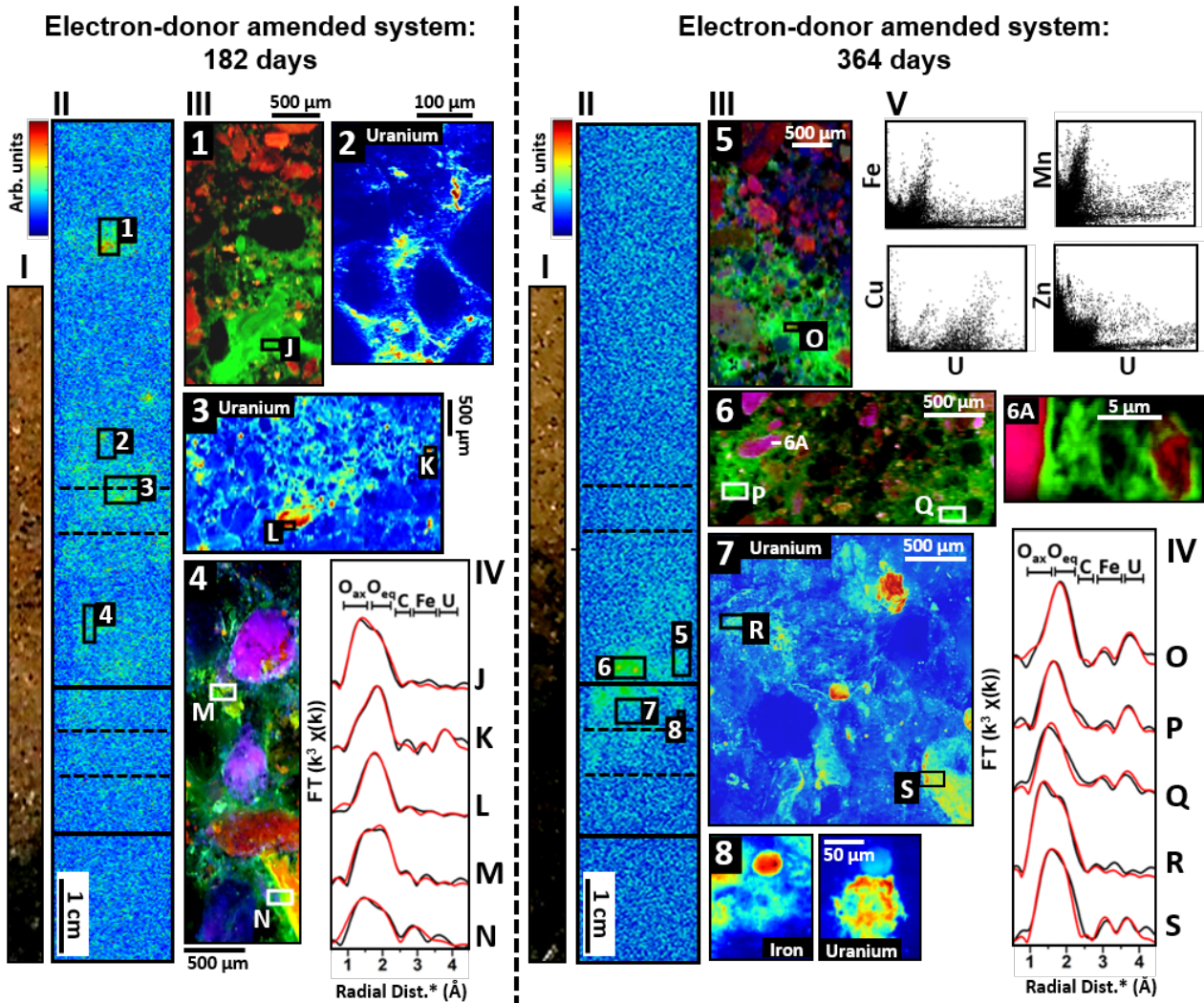
Figure 4. For each timepoint (182- and 364-days) from the electron-donor amended column system: **(I)** Color photographs showing the sediment profiles (10 cm vertical). Note the ingrowth of FeS (blackening) along the flow direction (base to top). **(II)** Full-length autoradiographs of the resin-embedded, cross sectioned sediments showing radioactivity distribution in the columns (acquisition times varied for clarity, see SI Figure S11 for U concentrations in digests). Solid horizontal lines denote the region of initial metaschoepite source emplacement, dashed horizontal lines denote the horizons from which bulk U L_{III}-edge XANES and EXAFS data were collected (Spectra B-E in relevant Figures and Tables). Numbered boxes within the autoradiographs correspond to μ-focus XRF maps in **(III)**. Maps in **(III)** are either displayed as element-specific color panels (where warmer colors denote relative higher concentrations) or as multi-element RGB maps (where green = U, red = Fe, blue = Mn, and color intensity denotes relative proportions of each element). XRF map 6A is a nano-focus map (pixel size 100 nm) of a FIB section extracted perpendicular to white line in XRF map 6 (see Figure S15 for details). Boxes marked J - S, within the XRF maps denote regions from which μ-focus U L_{III}-edge XAS data were collected, with EXAFS shown in **(IV)** (k^3 weighted Fourier transforms displayed for clarity, full datasets and XANES are presented in SI Section 9). *denotes that the Fourier transform is non-phase corrected. Bracketed regions above the plots show the expected peak positions for O, C and Fe and U scatterers (non-phase corrected). **(V)** Scatter plots denote correlations between major elements (Fe, Mn, Zn, Cu) and U from broad-scale maps over areas that encompass those shown. Positive correlations denote co-location of the elements at differing concentrations.

21

448   After 364-days, most of the U retained on the sediments was largely present in a discrete horizon ~1 cm

449   above the initial metaschoepite source. Here, some U was co-located with Fe-rich mineral grains (Figure 4;

450   maps 6 and 7), indicating that U may interact with reactive Fe at mineral surfaces. A proportion of the U was

451   also matrix-bound (i.e. not associated with mineral surfaces), possibly being retained by clays and/or organic

452   matter along groundwater flow paths (Figure 4, map 7).

453   µXANES measurements from the 182-day, electron-donor amended system (Figure S11, spectra J-N) showed

454   that U(IV) accounted for 40-60% of the U on the solid phase. µEXAFS also revealed a range of mixed

455   U(IV)/U(VI) species (Figure 4 and S13, Table S6). Structures indicative of non-crystalline U(IV) could be

456   modelled for several spectra. Only spectrum K, collected from a U hotspot ~7.5 cm from the sediment base,

457   could be confidently modelled using a U-U backscatter. Most spectra collected from the 182-day thin-section

458   could be modelled with C and/or Fe backscattering shells (Table S6). Combined, the bulk and µEXAFS data

459   suggest that monomeric U dominates in this sediment system during the early stages of bioreduction. Again,

460   Fe surfaces have also been implicated as important sites for both U(IV) and U(VI) retention.[71]

461   After 364-days in the electron-donor amended system, the residual U in the column was primarily contained

462   within the black-colored zones where sulfate reduction had occurred (Figure 4). The proportion of U(IV) in

463   this region, as modelled from the µXANES data (Figure S11, spectra O-S), was higher (63-80%) likely due to

464   longer periods under reducing conditions. Corresponding µEXAFS data (Figures 3 and S13; Table S7) were

465   best modelled with small contributions from uranyl-like O backscatters emphasizing that only residual U(VI)

466   remained in this system. Backscattering shells of C and/or Fe and increased contributions from UO_2 like U-U

467   backscatters could also be modelled. For example, spectra O, P, Q, and S (Figure 4) could all be modelled with

468   a U-U path concurrent with nano-crystalline, biogenic UO_2. Evidence for non-crystalline U(IV) in these

469   horizons was scarce; only spectrum R (65% U(IV)) showed no evidence of a U-U scattering contribution. When

470   considered alongside the bulk EXAFS data for this column system, it appears there is a preferential growth of

471   nano-crystalline UO_2 near the base of this system with sustained bioreduction.

472   Mechanisms for the preferential formation of 'monomeric' U(IV) vs. biogenic UO_2 are complex. Studies have

473   shown the end-product of microbial U(VI) reduction to be dependent both upon the local microbiology and

474   geochemistry. Indeed, systems containing higher ionic strength media (elevated concentrations of chlorides

475   and phosphates) have yielded an increased contribution from non-crystalline U(IV) from the same

476   bioreducing cell cultures.[10,11,62] Studies have also suggested that UO_2 formation is prohibited due to the

477   retention of U by cell biomass during reduction.[11,64] In phosphate-free systems, Gram-positive bacteria

478   preferentially produced non-crystalline U(IV) in direct contrast to Gram-negative bacteria, which produced

479   nano-particulate UO_2 under the same conditions, the differences proposed to be a result of cell envelope

480   architecture.[62] The formation of discrete U(IV) phosphate and carbonate phases must also be considered in

481   dynamic systems like those presented here, although no evidence is apparent in the μEXAFS, and no P was

482   supplied in the groundwater. Significant variations in binding site, local biomass, local porewater chemistry,

483   and microbiology are therefore competing factors within discrete micro-environments to favor the formation

484   of a specific end-member. Here, the interplay of all these factors on the micro-to-nano scale must be

485   considered, however it is difficult to isolate a specific mechanism of non-crystalline U(IV) formation in these

486   dynamic systems. In this case, as observed previously, [72,61] residence time (i.e. ageing of the non-crystalline

487   U(IV) fraction) likely accounts for the increase in nano-crystalline UO_2.

488   **Nano-focus XRF and XANES mapping**

489   Variations in U speciation were also present at the nanometer scale (Figure S14). The extraction of a wafer

490   of U contaminated sediment from the electron-donor amended column sediment (364-day) thin-section,

491   along a Fe-oxide grain boundary (Figure 4, map 6A), permitted nano-XRF and XANES mapping at the newly

492   commissioned Diamond Light Source Hard X-ray Nanoprobe (Figure S14). Discrete U L_{III}-edge XANES data

493   from this sample have been grouped by subtle differences in the spectra, and the result is a nanometer-scale

494   U speciation map. Figure S14 indicates the presence of up to three discrete groups of spectra identified within

495   the 10 μm x 5 μm FIB section; the most oxidized (blue and green) are more closely associated with the regions

496   of highest U concentration, along the boundaries of Fe-oxide grains.

Implications

This work has shown that an array of competing mechanisms control U migration and fate in complex sediment systems during metaschoepite dissolution. Under oxic conditions, metaschoepite dissolution resulted in significant $U(VI)_{(aq)}$ transport; however, U(VI) reaction with Fe-bearing sediment species retarded groundwater U transport and resulted in long-term (~1-year) U(VI) retention. During metaschoepite dissolution under anoxic conditions, significant amounts of UO_2-like colloids were produced. As colloids are known to enhance contaminant transport through the geosphere, this finding may be significant (e.g. for the management of sites contaminated with depleted U penetrators, mining sites, or for the geodisposal of metaschoepite containing wastes). However, further work is required to document the colloid formation mechanism(s) and stability, and this should include defining the role that the solid U source (i.e. chemical composition, surface morphology etc.) plays in controlling / instigating U colloid production, and the relative importance of biotic[46,48] vs. abiotic[49,52] UO_2 colloid formation mechanisms. Under anoxic conditions, micro-to-nano-focus XAS also revealed that U(VI), non-crystalline U(IV), and UO_2 were all retained in the sediment after metaschoepite dissolution, and UO_2 appeared to be a more important U(IV) product with added time. This may be significant in terms of uranium's general biogeochemistry, as it is thought that UO_2 may be more resistant to oxidative remobilisation, but clearly in this study, this is tensioned against significant U(IV) colloid production. Combined, the results highlight the complexity of U biogeochemistry in dynamic, evolving, environmental systems. This complexity, and how it can be modelled at the macro-scale, needs to be considered for contaminated sites and in nuclear waste disposal.

SUPPORTING INFORMATION

Contains additional information on sediment, groundwater, metaschoepite, and microbial community

characterization / composition, methods / techniques, pH data, and XAS data.

REFERENCES

1. Falck, W. E. Radioactive and other environmental contamination from uranium mining and milling. In *Environmental Remediation and Restoration of Contaminated Nuclear and Norm Sites*, **2015**, 3-34.

2. Salbu, B.; Janssens, K.; Lind, O. C.; Proost, K.; Danesi, P. R. Oxidation states of uranium in DU particles from Kosovo. *J. Environ. Radio.* **2003**, 64 (2-3), 167-173.

3. Handley-Sidhu, S.; Keith-Roach, M. J.; Lloyd, J. R.; Vaughan, D. J. A review of the environmental corrosion, fate and bioavailability of munitions grade depleted uranium. *Sci. Tot. Environ.* **2010**, 408 (23), 5690-5700.

4. Gavrilescu, M.; Pavel, L. V.; Cretescu, I. Characterization and remediation of soils contaminated with uranium. *J. Haz. Mat.* **2009**, 163 (2-3), 475-510.

5. Newsome, L.; Morris, K.; Lloyd, J. R. The biogeochemistry and bioremediation of uranium and other priority radionuclides. *Chem. Geol*. **2014**, 363, 164-184.

6. Morris, K.; Law, G. T. W.; Bryan, N. D., Chapter 6. Geodisposal of Higher Activity Wastes. In *Nuclear Power and the Environment*, **2011**; 129-151.

7. Nuclear Decommissioning Authority. *Geological disposal- investigating the implications of managing depleted, natural and low enriched uranium through geological disposal: progress report*; NDA/RWM/123; **2015**.

8. Brugge, D.; de Lemos, J. L.; Oldmixon, B. Exposure Pathways and Health Effects Associated with Chemical and Radiological Toxicity of Natural Uranium: A Review. *Rev. Environ. H*. **2005**, 20 (3), 177-193.

9. Craft, E.; Abu-Qare, A.; Flaherty, M.; Garofolo, M.; Rincavage, H.; Abou-Donia, M., Depleted and natural uranium: chemistry and toxicological effects. *J. Toxicol. Environ. Health. B. Crit. Rev.* **2004**, 7 (4), 297-317.

10. Alessi, D. S.; Uster, B.; Veeramani, H.; Suvorova, E. I.; Lezama-Pacheco, J. S.; Stubbs, J. E.; Bargar, J. R.; Bernier-Latmani, R. Quantitative separation of monomeric U(IV) from UO2 in products of U(VI) reduction. *Environ. Sci. Technol.* **2012**, 46 (11), 6150-6157.

554 11. Bernier-Latmani, R.; Veeramani, H.; Vecchia, E. D.; Junier, P.; Lezama-Pacheco, J. S.; Suvorova, E. I.;
555 Sharp, J. O.; Wigginton, N. S.; Bargar, J. R. Non-uraninite products of microbial U(VI) reduction. *Environ. Sci.*
556 *Technol.* **2010**, 44 (24), 9456-9462.

557 12. Bhattacharyya, A.; Campbell, K. M.; Kelly, S. D.; Roebbert, Y.; Weyer, S.; Bernier-Latmani, R.; Borch, T.
558 Biogenic non-crystalline U(IV) revealed as major component in uranium ore deposits. *Nat. Commun*. **2017**,
559 8, 15538.

560 13. Renshaw, J. C.; Butchins, L. J.; Livens, F. R.; May, I.; Charnock, J. M.; Lloyd, J. R. Bioreduction of uranium:
561 environmental implications of a pentavalent intermediate. *Environ. Sci. Technol*. **2005**, 39 (15), 5657-5660.

562 14. Steele, H.; Taylor, R. J. A theoretical study of the inner-sphere disproportionation reaction mechanism
563 of the pentavalent actinyl ions. *Inorg. Chem*. **2007**, 46 (16), 6311-6318.

564 15. Barnett, M. O.; Jardine, P. M.; Brooks, S. C. U(VI) adsorption to heterogeneous subsurface media:
565 application of a surface complexation model. *Environ. Sci. Technol*. **2002**, 36 (5), 937-942.

566 16. Brookshaw, D. R.; Pattrick, R. A.; Bots, P.; Law, G. T.W.; Lloyd, J. R.; Mosselmans, J. F.; Vaughan, D. J.;
567 Dardenne, K.; Morris, K. Redox interactions of Tc(VII), U(VI), and Np(V) with microbially reduced biotite and
568 chlorite. *Environ. Sci. Technol.* **2015**, 49 (22), 13139-13148.

569 17. Fuller, C. C.; Bargar, J. R.; Davis, J. A.; Piana, M. J. Mechanisms of uranium interactions with
570 hydroxyapatite: implications for groundwater remediation. *Environ. Sci. Technol*. **2002**, 36 (2), 158-165.

571 18. Livens, F. R.; Jones, M. J.; Hynes, A. J.; Charnock, J. M.; Mosselmans, J. F.; Hennig, C.; Steele, H.; Collison,
572 D.; Vaughan, D. J.; Pattrick, R. A.; Reed, W. A.; Moyes, L. N. X-ray absorption spectroscopy studies of
573 reactions of technetium, uranium and neptunium with mackinawite. *J. Environ. Radio.* **2004**, 74 (1-3), 211-
574 219.

575 19. Othmane, G.; Allard, T.; Morin, G.; Selo, M.; Brest, J.; Llorens, I.; Chen, N.; Bargar, J. R.; Fayek, M.; Calas,
576 G. Uranium association with iron-bearing phases in mill tailings from Gunnar, Canada. *Environ. Sci. Technol*.
577 **2013**, 47 (22), 12695-12702.

578 20. Um, W.; Serne, R. J.; Brown, C. F.; Last, G. V., U(VI) adsorption on aquifer sediments at the Hanford Site.
579 *J. Contam. Hydrol.* **2007**, 93 (1-4), 255-269.

580 21. Wang, Z.; Lee, S. W.; Catalano, J. G.; Lezama-Pacheco, J. S.; Bargar, J. R.; Tebo, B. M.; Giammar, D. E.
581 Adsorption of uranium(VI) to manganese oxides: X-ray absorption spectroscopy and surface complexation
582 modeling. *Environ. Sci. Technol*. **2013**, 47 (2), 850-858.

583 22. Kulkarni, S.; Misra, C. S.; Gupta, A.; Ballal, A.; Apte, S. K. Interaction of Uranium with Bacterial Cell
584 Surfaces: Inferences from Phosphatase-Mediated Uranium Precipitation. *Appl. Environ. Microbiol*. **2016**, 82
585 (16), 4965-4974.

586 23. Hennig, C.; Panak, P. J.; Reich, T.; Roßberg, A.; Raff, J.; Selenska-Pobell, S.; Matz, W.; Bucher, J. J.;
587 Bernhard, G.; Nitsche, H. EXAFS investigation of uranium(VI) complexes formed at Bacillus cereus and
588 Bacillus sphaericus surfaces. *Radiochim. Acta* **2001**, 89 (10), 625-631.

589 24. Roberts, H. E.; Morris, K.; Law, G. T. W.; Mosselmans, J. F. W.; Bots, P.; Kvashnina, K.; Shaw, S.
590 Uranium(V) incorporation mechanisms and stability in Fe(II)/Fe(III) (oxyhydr)oxides. *Environ. Sci. Technol.*
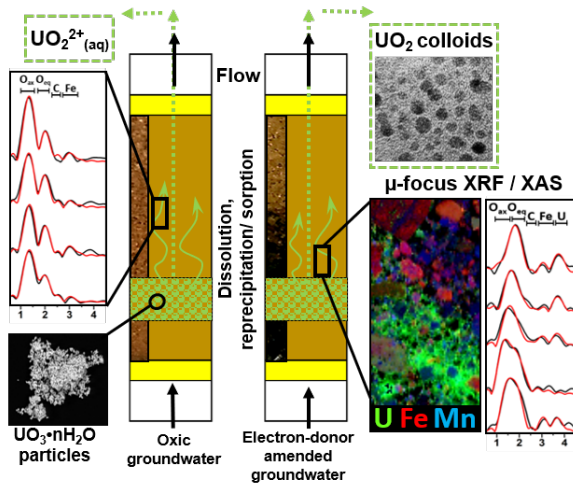591 *Lett.* **2017**, 4 (10), 421-426.

592 25. Marshall, T. A.; Morris, K.; Law, G. T. W.; Mosselmans, J. F. W.; Bots, P.; Roberts, H.; Shaw, S. Uranium
593 fate during crystallization of magnetite from ferrihydrite in conditions relevant to the disposal of
594 radioactive waste. *Min. Mag.* **2018**, 79 (06), 1265-1274.

595 26. Pidchenko, P.; Herberling, F.; Kvashnina, K.O.; Finck, N.; Bohnert, E.; Schäfer, T.; Rothe, J.; Geckeis, H.;
596 Vitova, T. Aqueous U(VI) interaction with magnetite nanoparticles in a mixed flow reaction system: HR-
597 XANES study. *J. Phys. Conf. Series.* **2016,** 712, 012086.

598 27. Wang, Y.; von Gunten, K.; Bartova, B.; Meisser, N.; Astner, M.; Burger, M.; Bernier-Latmani, R. Products
599 of in Situ Corrosion of Depleted Uranium Ammunition in Bosnia and Herzegovina Soils*. Environ. Sci.*
600 *Technol.* **2016**, 50 (22), 12266-12274.

601 28. Handley-Sidhu, S.; Bryan, N. D.; Worsfold, P. J.; Vaughan, D. J.; Livens, F. R.; Keith-Roach, M. J. Corrosion
602 and transport of depleted uranium in sand-rich environments*. Chemosphere* **2009**, 77 (10), 1434-1439.

603 29. Buck, B. J.; Brock, A. L.; Johnson, W. H.; Ulery, A. L. Corrosion of depleted uranium in an arid
604 environment: soil geomorphology, SEM/EDS, XRD and electron microprobe analyses. *Soil and Sediment*
605 *Contamination,* **2004**, 13, 545-561.

606 30. IAEA., Radioactive particles in the environment: sources, particle characterization and analytical
607 techniques. IAEA-TECDOC-1663, **2011**.

608 31. Finch, R. J.; Ewing, R. C. The corrosion of uraninite under oxidizing conditions. *Journal of Nuclear*
609 *Materials,* **1992**,190, 133-156.

610 31. Plášil, J. Oxidation–hydration weathering of uraninite: the current state-of-knowledge. *Journal of*
611 *Geosciences,* **2014**, 59, 99-114.

612 32. Salbu, B. Actinides associated with particles. *Radioactivity in the Environment* **2001**, 1, 121-138.

613 33. Walther, C.; Denecke, M. A., Actinide colloids and particles of environmental concern. *Chem. Rev*. **2013**,
614 113 (2), 995-1015.

615 34. Department for Energy and Climate Change, Implementing geological disposal; URN 14D/235; **2014**.

616 35. Law, G. T.W.; Geissler, A.; Boothman, C.; Burke, I. T.; Livens, F. R.; Lloyd, J. R.; Morris, K. Role of nitrate
617 in conditioning aquifer sediments for technetium bioreduction. *Environ. Sci. Technol*. **2010**, 44 (1), 150-155.

618 36. Wilkins, M. J.; Livens, F. R.; Vaughan, D. J.; Beadle, I.; Lloyd, J. R. The influence of microbial redox cycling
619 on radionuclide mobility in the subsurface at a low-level radioactive waste storage site. *Geobiol*. **2007**, 5 (3),
620 293-301.

621 37. Thorpe, C. L.; Lloyd, J. R.; Law, G. T. W.; Williams, H. A.; Atherton, N.; Cruickshank, J. H.; Morris, K.
622 Retention of 99mTc at ultra-trace levels in flowing column experiments – insights into bioreduction and
623 biomineralization for remediation at nuclear facilities. *Geomic. J.* **2016**, 33 (3-4), 199-205.

624 38. Masters-Waage, N. K.; Morris, K.; Lloyd, J. R.; Shaw, S.; Mosselmans, J. F. W.; Boothman, C.; Bots, P.;
625 Rizoulis, A.; Livens, F. R.; Law, G. T. W. Impacts of Repeated Redox Cycling on Technetium Mobility in the
626 Environment. *Environ. Sci. Technol.* **2017**, 51 (24), 14301-14310.

627 39. Viollier, E.; Inglett, P. W.; Hunter, K.; Roychoudhury, A. N.; Van Cappellen, P. The ferrozine method
628 revisited: Fe(II)/Fe(III) determination in natural waters. *Appl. Geochem.* **2000**, 15 (6), 785-790.

629 40. Jilbert, T.; de Lange, G.; Reichart, G.-J. Fluid displacive resin embedding of laminated sediments:
630 preserving trace metals for high-resolution paleoclimate investigations. *Limnol. Ocean. Meth.* **2008**, 6 (1),
631 16-22.

632 41. Jones, D. L.; Andrews, M. B.; Swinburne, A. N.; Botchway, S. W.; Ward, A. D.; Lloyd, J. R.; Natrajan, L. S.
633 Fluorescence spectroscopy and microscopy as tools for monitoring redox transformations of uranium in
634 biological systems. *Chem. Sci.* **2015**, 6 (9), 5133-5138.

635 42. Neill, T. S.; Morris, K.; Pearce, C. I.; Sherriff, N. K.; Burke, M. G.; Chater, P. A.; Janssen, A.; Natrajan, L.;
636 Shaw, S., Stability, composition, and core-shell particle structure of uranium(IV)-silicate colloids. *Environ.*
637 *Sci. Technol.* **2018**, 52 (16), 9118-9127.

638 43. Schindelin, J.; Arganda-Carreras, I.; Frise, E.; Kaynig, V.; Longair, M.; Pietzsch, T.; Preibisch, S.; Rueden,
639 C.; Saalfeld, S.; Schmid, B.; Tinevez, J. Y.; White, D. J.; Hartenstein, V.; Eliceiri, K.; Tomancak, P.; Cardona, A.
640 Fiji: an open-source platform for biological-image analysis. *Nat. Methods* **2012**, 9 (7), 676-682.

641 44. Stanley, D. M.; Wilkin, R. T. Solution equilibria of uranyl minerals: Role of the common groundwater
642 ions calcium and carbonate. J. Haz. Mat. **2019**, 377, 315-320.
643
644 45. Moore, K. T. X-ray and electron microscopy of actinide materials. *Micron*, **2010**, 41, 4, 336-358.

645 46. Suzuki, Y.; Kelly, S. D.;Kemner, K. M.; Banfield, J. F., Nanometre-size products of uranium bioreduction.
646 *Nature* **2002**, 419, 134.

647 47. Schofield E. J.; Veeramani H.; Sharp J. O.; Suvorova E.; Bernier-Latmani R.; Mehta A.; Stahlman J.; Webb
648 S. M.; Clark D. L.; Conradson S. D.; Ilton E. S.; Bargar J. R. Structure of biogenic uraninite produced by
649 Shewanella oneidensis strain MR-1. *Environ. Sci. Technol.* **2008**, 42, 21, 7898-7904.

650 48. Lee, S. Y.; Baik, M. H.; Choi, J. W. Biogenic formation and growth of uraninite (UO(2)). *Environ. Sci.*
651 *Technol.* **2010**, 44 (22), 8409-8414.

652 49. Lee, S. Y.; Cha, W. S.; Kim, J.-G.; Baik, M. H.; Jung, E. C.; Jeong, J. T.; Kim, K.; Chung, S. Y.; Lee, Y. J.,
653 Uranium(IV) remobilization under sulfate reducing conditions. *Chem. Geol.* **2014**, 370, 40-48.

654 50. Xie, J.; Lin, J.; Zhou, X. pH-dependent microbial reduction of uranium(VI) in carbonate-free solutions:
655 UV-vis, XPS, TEM, and thermodynamic studies. *Environ. Sci. Pollut. Res. Int.* **2018**, 25(22), 22308-22317.

656 51. Kaminski, M. D.; Dimitrijevic, N. M.; Mertz, C. J.; Goldberg, M. M. Colloids from the aqueous corrosion
657 of uranium nuclear fuel. *J. Nuc. Mats.* **2005**, 347 (1-2), 77-87.

658 52. O'Loughlin, E. J.; Kelly, S. D.; Cook, R. E.; Csencsits, R.; Kemner, K. M. Reduction of uranium(VI) by mixed
659 iron(II)/iron(III) hydroxide (green rust): formation of UO2 nanoparticles. *Environ. Sci. Technol.* **2003**, 37(4),
660 721-727.

661 53. Leinders, G.; Cardinaels, T.; Binnemans, K.; Verwerft, M. Accurate lattice parameter measurements of
662 stoichiometric uranium dioxide. *J. Nuc. Mats.* **2015**, 459, 135-142.

663 54. Van Bodegom, P. M.; van Reeven, J.; Denier van der Gon, H. A. C. Prediction of reducible soil iron from
664 iron extraction data. *Biogeochem.* **2003**, 64 (2), 231-245.

665 55. Rossberg, A.; Reich, T.; Bernhard, G. Complexation of uranium(VI) with protocatechuic acid-application
666 of iterative transformation factor analysis to EXAFS spectroscopy. *Anal. Bioanal. Chem.* **2003**, 376 (5), 631-
667 638.

668 56. Bargar, J. R.; Reitmeyer, R.; Davis, J. A., Spectroscopic confirmation of uranium(VI)–carbonato
669 adsorption complexes on hematite. *Environ. Sci. Technol.* **1999**, 33 (14), 2481-2484.

670 57. Moyes, L. N.; Parkman, R. H.; Charnock, J. M.; Vaughan, D. J.; Livens, F. R.; Hughes, C. R.; Braithwaite, A.
671 Uranium uptake from aqueous solution by interaction with goethite, lepidocrocite, muscovite, and
672 mackinawite: an X-ray absorption spectroscopy study. *Environ. Sci. Technol.* **2000**, 34 (6), 1062-1068.

673 58. Singh, A.; Catalano, J. G.; Ulrich, K. U.; Giammar, D. E. Molecular-scale structure of uranium(VI)
674 immobilized with goethite and phosphate. *Environ. Sci. Technol.* **2012**, 46 (12), 6594-6603.

675 59. Waite, T. D.; Davis, J. A.; Payne, T. E.; Waychunas, G. A.; Xu, N. Uranium(VI) adsorption to ferrihydrite:
676 application of a surface complexation model. *Geochim. Cosmochim. Acta.* **1994**, 58 (24), 5465-5478.

677 60. Winstanley, E. H.; Morris, K.; Abrahamsen-Mills, L. G.; Blackham, R.; Shaw, S., U(VI) sorption during
678 ferrihydrite formation: Underpinning radioactive effluent treatment. *J. Haz. Mat.* **2019**, 366, 98-104.

679 61. Newsome, L.; Morris, K.; Shaw, S.; Trivedi, D.; Lloyd, J. R. The stability of microbially reduced U(IV);
680 impact of residual electron donor and sediment ageing. *Chem. Geol.* **2015**, 409, 125-135.

681 62. Boyanov, M. I.; Fletcher, K. E.; Kwon, M. J.; Rui, X.; O'Loughlin, E. J.; Loffler, F. E.; Kemner, K. M. Solution
682 and microbial controls on the formation of reduced U(IV) species. *Environ. Sci. Technol*. **2011**, 45 (19), 8336-
683 8344.

684 63. Veeramani, H.; Alessi, D. S.; Suvorova, E.; Lezama Pacheco, J. S.; Stubbs, J. E.; Sharp, J. O.; Dippon, U.;
685 Kappler, A.; Bargar, J. R.; Bernier-Latmani, R. Products of abiotic U(VI) reduction by biogenic magnetite and
686 vivianite. *Geochim. Cosmochim. Acta.* **2011**, 75 (9), 2512-2528.

687 64. Bargar, J. R.; Williams, K. H.; Campbell, K. M.; Long, P. E.; Stubbs, J. E.; Suvorova, E.; Lezama Pacheco, J.
688 S.; Alessi, D. S.; Webb, S. M.; Davis, J. A.; Giammar, D. E.; Blue, L. Y.; Bernier-Latmani, R. Uranium redox
689 transition pathways in acetate-amended sediments. *PNAS* **2013**, 110 (12), 4506-4511.

690 65. Cumberland, S. A.; Douglas, G.; Grice, K.; Moreau, J. W. Uranium mobility in organic matter-rich
691 sediments: A review of geological and geochemical processes. *E. Sci. Rev.* **2016**, 159, 160-185.

692 66. Hafeez, B.; Khanif, Y. M.; Saleem, M., Role of zinc in plant nutrition- a review. *A. J. Exp. Agric.* **2013**, 3
693 (2), 374-391.

694 67. Yamasaki, H.; Pilon, M.; Shikanai, T., How do plants respond to copper deficiency? *Plant Signa. Beh.*
695 **2008**, 4 (4), 231-232.

696 68. Boghi, A.; Roose, T.; Kirk, G. J. D. A Model of Uranium Uptake by Plant Roots Allowing for Root-Induced
697 Changes in the soil. *Environ. Sci. Technol.* **2018**, 52 (6), 3536-3545.

698 69. Li, D.; Kaplan, D. I.; Chang, H. S.; Seaman, J. C.; Jaffe, P. R.; Koster van Groos, P.; Scheckel, K. G.; Segre, C.
699 U.; Chen, N.; Jiang, D. T.; Newville, M.; Lanzirotti, A. Spectroscopic evidence of uranium immobilization in
700 acidic wetlands by natural organic matter and plant roots. *Environ. Sci. Technol.* **2015**, 49 (5), 2823-2832.

701 70. Savenko, A. V., Sorption of UO22+ on calcium carbonate. *Radiochemistry* **2001**, 43 (2), 193-196.

702 71. Latta, D. E.; Mishra, B.; Cook, R. E.; Kemner, K. M.; Boyanov, M. I. Stable U(IV) complexes form at high-
703 affinity mineral surface sites. *Environ. Sci. Technol.* **2014**, 48 (3), 1683-1691.

704 72. Stylo, M.; Alessi, D. S.; Shao, P. P.; Lezama-Pacheco, J. S.; Bargar, J. R.; Bernier-Latmani, R.
705 Biogeochemical controls on the product of microbial U(VI) reduction. *Environ. Sci. Technol.* **2013**, 47 (21),
706 12351-12358.

--TOC ART--